

## Sensitivity of Radiative–Convective Equilibrium Simulations to Horizontal Resolution

OLIVIER PAULUIS

*Courant Institute of Mathematical Sciences, New York University, New York, New York*

STEPHEN GARNER

*NOAA/Geophysical Fluid Dynamics Laboratory, Princeton, New Jersey*

(Manuscript received 7 January 2005, in final form 3 November 2005)

### ABSTRACT

This paper investigates the impacts of horizontal resolution on the statistical behavior of convection. An idealized radiative–convective equilibrium is simulated for model resolutions ranging between 2 and 50 km. The simulations are compared based upon the analysis of the mean state, the energy and water vapor transport, and the probability distribution functions for various quantities. It is shown that, at a coarse resolution, the model is unable to capture the mixing associated with shallow clouds. This results in a dry bias in the lower troposphere, and in an excessive amount of water clouds. Despite this deficiency, the coarse resolution simulations are able to reproduce reasonably well the statistical properties of deep convective towers. This is particularly apparent in the cloud ice and vertical velocity distributions that exhibit a very robust behavior.

A theoretical scaling for the vertical velocity as function of the grid resolution is derived based upon the behavior of an idealized air bubble. It is shown that the vertical velocity of an ascending air parcel is determined by its aspect ratio, with a wide, flat parcel rising at a much slower pace than a narrow one. This theoretical scaling law exhibits a similar sensitivity to that of the numerical simulations. It is used to renormalize the probability distribution functions for vertical velocity, which show a very good agreement for resolutions up to 16 km. This new scaling law offers a way to improve direct simulations of deep convection in coarse resolution models.

---

### 1. Introduction

Deep convection is a key element of the climate system, not only because of its role in controlling the lapse rate in the Tropics, but through its impact on the cloud field and radiative fluxes. Hence, the representation of convection is a crucial aspect of any climate model. In traditional general circulation models (GCMs), the horizontal resolution is of the order of 100 km. This prevents these models from directly simulating processes taking place at the convective scales. This limitation has been addressed over the years through the development of various cumulus parameterizations (Manabe et al. 1965; Arakawa and Schubert 1974; Betts and Miller 1986; Emanuel 1991; Arakawa 2004) whose main functions are to determine the effects of convec-

tion on the temperature, humidity, and clouds within an atmospheric column. However, these parameterizations cannot be derived from first principles, but rather must rely on a set of semiempirical closure assumptions about the behavior of convective systems. As such, the necessary use of cumulus parameterizations in GCMs remains one of the largest sources of uncertainty for our understanding of the climate system.

One possible solution to this issue is to increase the model's resolution in order to explicitly represent the scales at which convection takes place. This is the approach taken by cloud system resolving models (CSRMs) to study the behavior of convective systems over limited areas. Satoh et al. (2005) have recently conducted a 3.5-km resolution global simulation with the Earth Simulator. Given the continuous increase in computing resources, it should be possible to run routinely a global CSRMs within the next decade. An intermediate approach is to replace the traditional cumulus parameterization with a reduced CSRMs calculation

---

*Corresponding author address:* O. Pauluis, Warren Weaver Hall, 251 Mercer Street, New York, NY 10012-1185.  
E-mail: pauluis@cims.nyu.edu

(Grabowski 2001; Randall et al. 2003). Both of these approaches rely on the implicit assumption that the behavior of convection can be accurately captured by a high-resolution model. However, as increasing model resolution is computationally expensive, one would like to determine the coarsest resolution possible that would properly capture the necessary physical processes.

The answer to such question depends critically on the feature of convection that one tries to replicate. For instance, Lorenz (1975) distinguishes between prediction of the first kind, which focuses on a specific trajectory of a dynamical system, and prediction of the second kind, which determines the statistical properties of the system attractor. As predictions of the first and second kinds are different problems, the corresponding resolution requirements might also be different. Weather forecasting, where one predicts the evolution of weather systems over a few days, is a prediction of the first kind. The conventional wisdom is that, for cloud system simulations and weather forecasting, CSRMs with a horizontal resolution of 2 km or less can capture the behavior of cloud systems (see, e.g., Redelsperger et al. 2000). Specific aspect of convection such as entrainment and shallow clouds might require even higher resolution. For example, Bryan et al. (2003) argue that resolution of 500 m or less might be required to reproduce the propagation of a squall line.

In climate models, the objective is to capture the impact of an ensemble of convective systems on the temperature, humidity, and energy of the atmosphere. This is inherently a prediction of the second kind, and the resolution requirements for a CSRMs in a climate application might not be the same as those for a weather forecasting model. A particular issue is whether the physical parameterizations of a CSRMs must be complemented by additional components (such as a deep convective parameterization) at intermediary resolution between the convective and mesoscale. Previous studies have offered different answers. Liu et al. (2001) observe that 3D simulation with 15-km resolution could reproduce reasonably well results from a 2D simulation with 2-km resolution, although they find some sensitivity for organized convection. In contrast, Jung and Arakawa (2004) find that, in 2D simulations, significant correction terms needed to be included for their coarse resolution (32 km) simulations to reproduce the results obtained with high resolution (2 km). The key questions here are to determine how CSRMs simulations converge with resolution, and whether additional parameterization would result in faster convergence.

The primary objective of this paper is to determine

the resolution requirement for CSRMs simulations for climate applications by investigating the impacts of a model resolution on the statistical behavior of convection. In the present paper, a CSRMs is used to simulate an idealized radiative–convective equilibrium with the horizontal resolution varying from 2 to 50 km. The model’s convergence is assessed by comparing the coarse resolution simulations with the 2-km reference case. This assessment focuses primarily on the statistical properties of the convective systems, by determining the sensitivity of the mean-state, convective transport, and distribution functions for vertical velocity and condensed water. The goal here is to evaluate the capability of coarse resolution simulations to capture various aspects of moist convection.

The numerical model and experimental design are described in section 2 and in the appendix. The model solves the equations of motion for a fully compressible atmosphere, with a parameterization for cloud microphysics. For this paper, the radiative transfer calculations have been replaced by an idealized cooling profile. As this prevents cloud–radiative feedbacks, the sensitivity in our simulations is primarily due to the internal dynamics of convective systems. Particular attention in the model development has been given to the advection scheme. After studying different options, the piecewise parabolic method (PPM; Colella and Woodward 1984) was selected. Apart from this specific choice for the advection scheme, the model dynamics should be representative of a wide range of compressible and anelastic atmospheric models.

The results from the simulations are presented in section 3. The behavior of convection is analyzed through a set of long-term statistics: mean temperature and humidity, convective heat and water transport, net latent heat release, and probability distribution functions for cloud water, cloud ice, and vertical velocity. It is shown that the horizontal resolution has a strong impact on the behavior of shallow convection, but that deep convective towers are only slightly affected. In particular, low-level humidity and cloud water are very sensitive to the horizontal resolution, while the vertical velocity and cloud ice exhibit a much more robust behavior, even for resolutions up to 16 km.

Section 4 provides a theoretical analysis of the sensitivity of the vertical velocity to horizontal resolution. A scaling argument is derived to explain the low sensitivity of the vertical velocity of deep convection to horizontal resolution. It is found that the vertical velocity of a 16-km simulation should be roughly half that of a 2-km simulation. The scaling argument can also be used to renormalize the vertical velocity probability distribution so that coarse resolution simulations can be

used to predict the behavior of high-resolution simulations. It is found that the low sensitivity of the vertical velocity to the horizontal resolution is a characteristic of the nonhydrostatic convection, and could potentially be used to improve coarse resolution simulations. Section 5 discusses further the implications of this study for explicit simulations of deep convection in global models.

## 2. Model and experiment

### a. Model

The model used here has been developed at Geophysical Fluid Dynamics Laboratory (GFDL) through a collaboration between Steve Garner, Olivier Pauluis, Chris Kerr, and Isidoro Orlanski. The numerical model is composed of three main components: 1) a compressible dynamical core, which solves the equation of motion for moist air, 2) a bulk microphysical parameterization that determines the conversion rates of the different types of water, and the associated latent heat release, and 3) a set of physical parameterizations shared with the GFDL climate model (Anderson et al. 2004).

The prognostic variables of the dynamical core are the three-dimensional velocity  $u$ ,  $v$ ,  $w$ , the potential temperature  $\theta$ , specific humidity  $q_v$ , five different species of condensed water (cloud water, cloud ice, rain, snow, and graupel), and the Exner function  $\pi = (p/p_0)^{(R/C_p)}$ , where  $p_0$  is an arbitrary reference pressure,  $R$  is the gas constant, and  $C_p$  is the specific heat at constant pressure of dry air. The density of moist air  $\rho$  is not a prognostic variable, but is obtained from the ideal gas law.

The numerical aspects of the model are detailed in the appendix. The model uses a time-splitting technique, with a long time step for advection and physics, and with a shorter time-step for the sound and gravity waves. Advective tendencies are obtained by using the PPM in all three directions for all variables (Colella and Woodward 1984). The microphysical parameterization of Lin et al. (1983), with subsequent modifications by Lord et al. (1984), and Krueger et al. (1995) is used here. It separates condensed water is separated into five different species, cloud water, cloud ice, rainwater, snow, and graupel, and is used to compute the transformation rate between the different water types, as well as the corresponding temperature change. While a wide selection of additional physical parameterizations is available through the GFDL Flexible Modeling System (FMS), this study is focused on numerical convergence, and the simplest configuration is favored. The physical parameterizations used here are limited to a

Monin–Obukhov similarity for the surface flux, and a three-dimensional turbulent kinetic energy scheme. A sponge layer at the upper boundary dampens vertically propagating sound and gravity waves. No parameterization for either shallow or deep convection has been used.

### b. Experimental design

The nonhydrostatic model is used to simulate an idealized radiative–convective equilibrium. The atmosphere is destabilized through a combination of surface heating and tropospheric cooling. This initiates convection and, after some time, the system reaches a statistical equilibrium where convective systems continuously form, grow, and decay. The primary advantage of the radiative–convective equilibrium lies in that it is the simplest experimental setup to simulate active convection forced by an external influence—in this case the differential heating. By limiting oneself to a horizontally uniform domain, one greatly simplifies the problem, which can be then be studied on a relatively small domain (a few hundred kilometers in both horizontal directions are sufficient if one uses a doubly periodic domain). The main drawback is that it is not possible to account for the interaction between convection and the planetary circulation.

The atmosphere is destabilized by a combination of surface heat flux and tropospheric cooling. The surface forcings are obtained by assuming that the lower boundary is an ocean at a constant temperature of 301.5 K. The tropospheric cooling is determined from an idealized cooling profile rather than an explicit radiative transfer calculation. The cooling rate is given by

$$\partial_t T|_{\text{cool}} = -1.5 \text{ K day}^{-1} \quad \text{for } T > 207.5 \text{ K} \quad (1)$$

$$= \frac{200 \text{ K} - T}{5 \text{ day}} \quad \text{elsewhere.} \quad (2)$$

This produces a uniform cooling of  $1.5 \text{ K day}^{-1}$  within most of the troposphere while maintaining the stratosphere at a uniform temperature of 200 K. The idealized cooling does not account for the interactions between cloud and radiation, which play an important role both for the behavior of convective systems and for the energy budget of the atmosphere. The choice in this study is to favor simplicity, and to focus primarily on the interaction between dynamics and thermodynamics. An investigation of the sensitivity of the cloud radiative feedbacks to horizontal resolution is left to a future study.

Radiative–convective equilibrium is simulated on a three-dimensional, double periodic domain. The simu-

lations are repeated for resolution of 2, 4, 6, 8, 12, 16, 25, and 50 km. The 2-km simulation is used as a reference, and is performed on a 200 km × 200 km horizontal domain with 100 × 100 grid points. All other simulations use a 50 × 50 horizontal grid. This implies that the physical domain is the same for the 2- and 4-km resolution cases, and becomes larger at coarser resolution. All the experiments here use the same vertical grid—a 60-point stretched grid with resolution of 100 m near the surface and 700 m at the top (25 km). The model did not use any numerical diffusion, as these are not required because of the monotonicity of the PPM advection scheme.

**3. Numerical results**

The model is integrated for a period of 16 days, with the analysis performed on the last 8 days of the simulations. While 16 days is probably too short for the model to reach radiative convective equilibrium, the initial conditions were obtained from a two-month integration with a 4-km resolution, and were already fairly close to the radiative–convective equilibrium state, at least in the 4-km case. The residual trends after 16 days are fairly small.

The precipitation rate varies from 4.45 mm day<sup>-1</sup> at 2-km resolution to 4.95 mm day<sup>-1</sup> at 50-km resolution. The latter is the only simulation that produced a precipitation rate greater than 4.7 mm day<sup>-1</sup>. In all cases, the atmosphere is close to a moist adiabatic. The convective available potential energy (CAPE) for a reversible ascent varies from 660 J kg<sup>-1</sup> at 12-km resolution to 870 J kg<sup>-1</sup> at 50-km resolution.

*a. Mean state*

Figure 1 shows the resolution dependence of the total moist static energy, total dry static energy, and total latent heat content. It indicates a systematic drying and warming at coarser resolution. The vertical structure of the drying is illustrated in Fig. 2, which shows the difference in horizontal mean specific humidity between different simulations and the 2-km control run. While simulations with 4- and 6-km resolution reproduce reasonably well the water vapor distribution of the control run, coarser resolution produces a very marked dry bias in the lower troposphere. The strongest drying occurs in the lower troposphere. In the first few hundred meters, which corresponds roughly to the subcloud layer, humidity exhibits the opposite tendency, with coarse resolution producing a moister boundary layer. The vertical structure of the temperature difference is shown in Fig. 3. This temperature structure corresponds

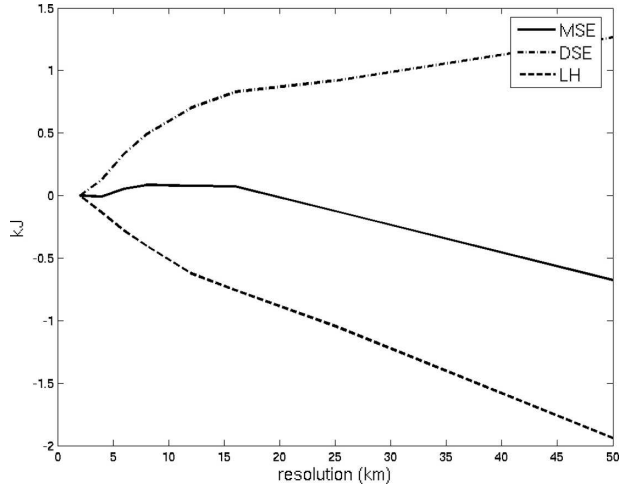


FIG. 1. Bias in mean moist static energy (solid line), mean dry static energy (dash–dotted line), and mean latent heat content (dash line) as function of the model’s resolution. The bias here is defined as the difference between the simulation and the reference 2-km simulation.

closely to a moist adiabat that matches the changes in the subcloud layer humidity. The biases in specific humidity and temperature are by far the most drastic impact of the horizontal resolution.

The humidity bias at coarse resolution can be interpreted as a result of a lack of mixing by shallow clouds. In these simulations, convective downdrafts generate cold pools that expand over areas much larger than the individual clouds. The expansion of the cold pools results in a continuous stirring within the subcloud layer,

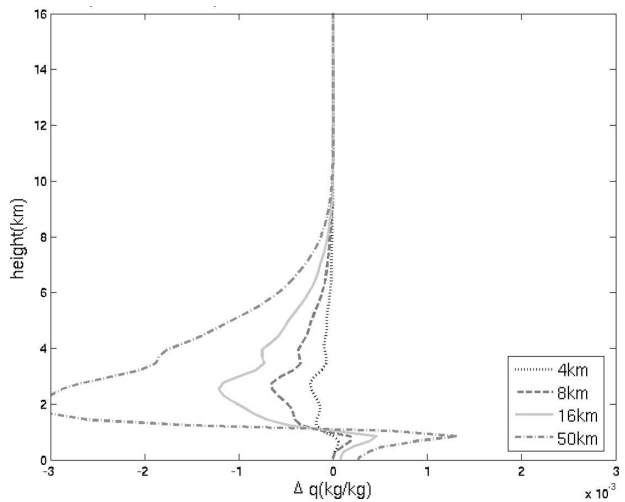


FIG. 2. Difference in horizontal mean specific humidity between different simulations and the 2-km control run for 4- (dotted line), 8- (dashed line), 16- (solid line), and 50-km (dash–dotted line) horizontal resolution.

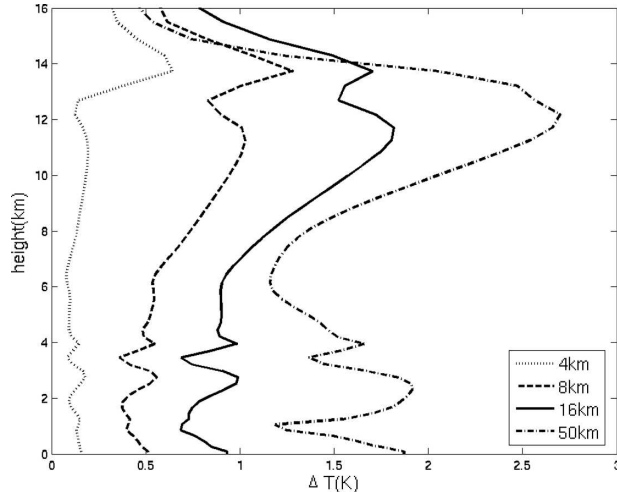


FIG. 3. Difference in horizontal mean temperature between different simulations and the 2-km control run for 4- (dotted line), 8- (dashed line), 16- (solid line), and 50-km (dash-dotted line) horizontal resolution.

and leads to the formation of a large number of shallow clouds primarily at the advancing edge of the cold pools. This mechanism is active at all resolutions, with the coarse simulation actually exhibiting a larger cloud cover at low levels (see section 3b). However, at the coarse resolution, the shallow clouds do not overturn or mix with environment. Instead, they dissipate by falling back into the boundary layer. In contrast, the 2- and 4-km experiments show a large number of shallow convective clouds that mix with their environment and humidify the lower troposphere. It should be emphasized that even a 2-km resolution is insufficient for an accurate representation of shallow convection. Hence, it is not surprising that changes in the horizontal resolution have a very marked impact on the dynamical behavior of simulated shallow clouds.

The temperature bias is also closely related to the humidity bias. Figure 1 shows that the vertically integrated moist static energy does not change as much as the dry static energy and the latent heat individually, particularly for resolutions finer than 20 km. The rate of change of the vertically integrated moist static energy is given by the difference between the total surface energy flux (i.e., sensible and latent heat fluxes) and the interior cooling, excluding the small contribution due to kinetic energy. As the simulations are near radiative-convective equilibrium, these are almost balanced, and there is little evolution of the moist static energy. Furthermore, surface fluxes and cooling rate are only weakly affected by the model resolution, the former through changes in the lowest level enthalpy and wind velocity, and the latter through changes in temperature.

As the energy sources and sinks are insensitive to the model resolution, one expects the integrated static energy to be similarly insensitive to the model resolution. If the total moist static energy were to be constant, a dry bias at coarse resolution, corresponding to a reduction of the latent heat content, would have to be balanced by an increase in the dry static energy, that is, an increase in temperature. From a mechanistic point of view, the reduction of the mixing by shallow convection in the coarse resolution simulation leads to a moistening of the boundary layer. This increases the convective precipitation, which in turn warms the troposphere.

The formulation of the cooling rate (1) is also partially responsible for the magnitude of the tropospheric warming in the steady state. Indeed, the cooling rate (1) is independent of the temperature through most of the atmosphere. The integrated cooling  $Q_{\text{cool}}$  depends primarily on the location of the 200-K isotherm, and its sensitivity to the mean atmospheric temperature  $T_{\text{atm}}$  is low:  $dQ_{\text{cool}}/dT_{\text{atm}} \approx 0.6 \text{ W m}^{-2} \text{ K}^{-1}$ . This is about 6 times smaller than sensitivity of the infrared radiation emitted by a blackbody at the same temperature as the atmosphere. This also implies a very long relaxation time for the temperature:  $\tau = C_p M (dQ_{\text{cool}}/dT_{\text{atm}})^{-1} \approx 200$  days ( $M$  is the atmospheric mass per unit area), which is much longer than the length of the experiments. Another formulation for the idealized cooling, such as a relaxation toward a specific temperature profile, would likely have resulted in significantly lower sensitivity for the tropospheric temperature.

While the mean state exhibits some sensitivity to the horizontal resolution, the tropospheric lapse rate is still close to a moist adiabat even at the coarsest resolution. This indicates that coarse convection remains very effective at controlling the tropospheric temperature. Indeed, as seen in section 3c, the vertical velocity in the 50-km resolution runs remains of the order of 2–3  $\text{m s}^{-1}$ , so that the corresponding convective overturning time of 1–2 h remains much shorter than the radiative cooling time. The primary limitation of a coarse simulation lies in its inability to represent the shallow clouds necessary to moisten the lower troposphere.

#### b. Convective energy transport

In radiative-convective equilibrium, the total energy transport by convection must balance the radiative cooling in the troposphere. As the imposed cooling profile has very little sensitivity to the model resolution, so does the total energy transport by convection. However, it is possible for the model resolution to affect the microphysical processes, and modify how the energy transport is partitioned between sensible and latent heat. Such change of the partitioning between sensible

and latent heat transport would imply a significant change in the behavior of convection. Pauluis and Held (2002a) show that the kinetic energy generated by convective motions is strongly reduced by irreversible entropy production due to diffusion of water vapor and irreversible phase changes. Furthermore, they show that impact of these moist processes on the generation of kinetic energy in the atmosphere is proportional to the latent heat transport. They define the effective temperature of latent heat release  $T_{\text{lat}}$  as

$$\frac{Q_{\text{lat}}}{T_{\text{lat}}} = \int \rho L_v \frac{C - E}{T}, \quad (3)$$

where  $Q_{\text{lat}} = \int \rho L_v (C - E)$  is the total latent heat release,  $C$  and  $E$  are the condensation and reevaporation rate, respectively, and  $L_v$  is the latent heat of vaporization. Pauluis and Held (2002b) show that the reduction of the kinetic energy production by the moist processes is approximately given by

$$\bar{T} \Delta S_{\text{irr}} \approx 0.75 Q_{\text{lat}} \frac{T_{\text{surf}} - T_{\text{lat}}}{\bar{T}}, \quad (4)$$

with  $\Delta S_{\text{irr}}$  the entropy production by diffusion of water vapor and irreversible phase changes,  $T_{\text{surf}}$  the surface temperature, and  $\bar{T}$  an average atmospheric temperature. In the simulations discussed in Pauluis and Held (2002a), moist processes account for two thirds of the entropy production in moist convection, which translates in a reduction of the kinetic energy generation of roughly  $10 \text{ W m}^{-2}$ . A change in the partitioning of the convective energy transport between latent and sensible heat would imply a change in the entropy production by moist processes (4) and henceforth the amount of kinetic energy generated by convective motions.

Figure 4 shows the horizontally averaged net condensation rate, which is not significantly affected by the model resolution. This ensures that through (3) and (4) that the total entropy production due to moist processes is not significantly affected by the change in resolution. This is further confirmed by Fig. 5, which shows the buoyancy flux in the model. The kinetic energy generation can be approximated by the integral of the buoyancy flux (see, e.g., the appendix of Emanuel and Bister 1996), and is remarkably insensitive to the model's resolution, with the net kinetic energy generation varying from  $1.7$  to  $1.8 \text{ W m}^{-2}$ . Altogether, this indicates that the thermodynamic behavior of deep convection is not significantly altered by changes in the model resolution.

*c. Statistical characteristics of convection*

One of the primary motivations for direct simulation of convection is to obtain a better statistical description

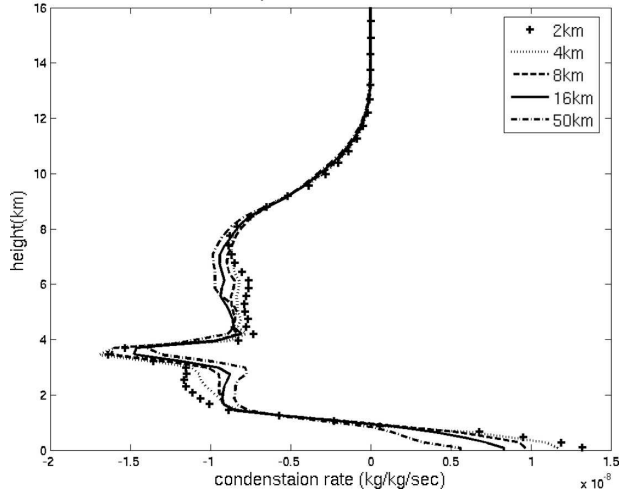


FIG. 4. Net source of water vapor due to microphysical transformation. Results shown for model resolution of 2 (cross), 4 (dotted line), 8 (dashed line), 16 (solid line), and 50 km (dash-dotted line).

of convective systems. Specifically, it is important to examine whether the coarse resolution can reproduce the probability distribution functions (PDFs) obtained at higher resolution. The PDFs presented here focus on the cloud water, cloud ice, and vertical velocity as indicators of the behavior of convective systems. Given the importance of cloud radiative feedbacks in the climate systems, the ability of a model to reproduce the properties of clouds is of particular interest here. In addition, as vertical velocity is one of the primary factors controlling the microphysical processes taking place within a given cloud, understanding how the reso-

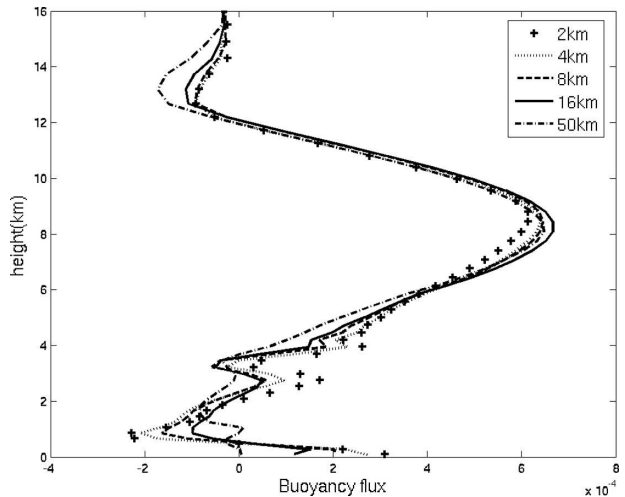


FIG. 5. Total buoyancy flux as function of height. Results shown for model resolution of 2 (cross line), 4 (dotted line), 8 (dashed line), 16 (solid line), and 50 km (dash-dotted line).

lution affects vertical velocity can offer insight on how to improve the representation of the cloud field in coarse resolution runs.

The PDFs for cloud water and ice are presented in Figs. 6 and 7 for different model resolutions. It is apparent that, at the coarsest resolution of 50 km, the model does not reproduce the PDFs from the reference case. For intermediate resolutions between 8 and 16 km, the model is able to capture several features of the cloud ice distribution, including the magnitude of the peak at  $0.6 \text{ g kg}^{-1}$ , and the tail of the distribution at large  $q_i$  associated with strong convective updrafts. There is a small bias at intermediary value of the cloud ice content  $0.3 < q_i < 0.5 \text{ g kg}^{-1}$  that could be associated with the behavior of decaying cirrus clouds. The cloud water distribution exhibits a much more marked bias, particularly in the range of  $0 < q_c < 0.5 \text{ g kg}^{-1}$ . Figure 8 shows the variation of the cloud fraction with height (the cloud fraction is defined here as the probability for the condensate mixing ratio to be larger than  $0.05 \text{ g kg}^{-1}$ ). Overall, the cloud ice fraction at high altitude can be reproduced within 25% margin with resolutions in the 8–16-km range, but low-level cloud water is more sensitive. The differences in cloud water PDFs are consistent with a longer decay time scale for shallow clouds at coarse resolution, and are most likely a consequence of the poor behavior of shallow convection, as discussed earlier in section 3a.

The amount of cloud ice is closely tied to the behavior of deep convective updrafts. One of the most remarkable features of the simulations is that coarse resolution runs do a very good job of reproducing the PDF

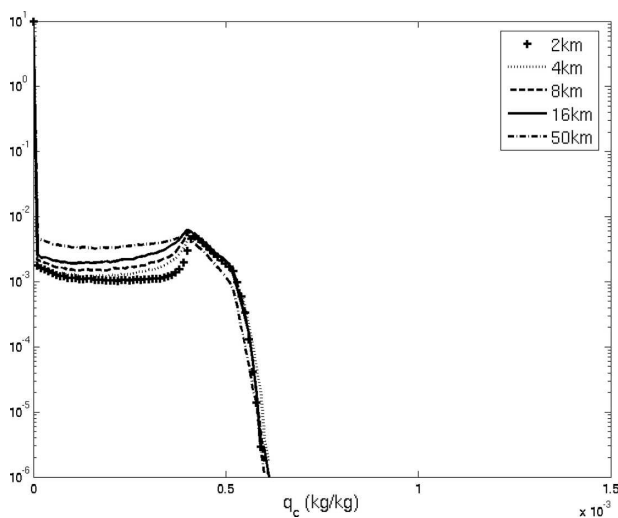


FIG. 6. PDF for cloud water for resolution of 2 (cross), 4 (dotted line), 8 (dashed line), 16 (solid line), and 50 km (dash-dotted line).

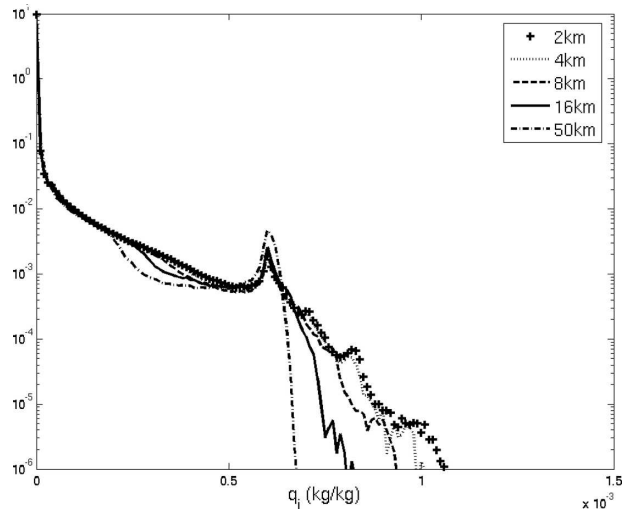


FIG. 7. PDF for cloud ice for resolution of 2 (cross), 4 (dotted line), 8 (dashed line), 16 (solid line), and 50 km (dash-dotted line).

for vertical velocity, as shown in Figs. 9 and 10. These PDFs have been constructed by sampling the vertical velocity at each level between 4 and 8 km, weighted by the mass of air in the grid box. The most significant difference occurs in the tail of the PDFs which exhibit a resolution-sensitive cutoff. Even for a resolution as coarse as 16 km, the vertical velocity remains about half as strong as the vertical velocity in the higher resolution simulations. This surprisingly robust behavior is analyzed in greater detail in section 4 of this paper.

The weak sensitivity of the vertical velocity to horizontal resolution is welcome news. The microphysical properties of clouds are strongly related to the vertical velocity experienced during their ascent, as it directly affects the conversion rates. The robust behavior of the vertical velocity also implies that the coarse resolution simulations should be able to reproduce the microphysical properties of deep convection reasonably well. It is not surprising that the PDFs for vertical velocity and cloud ice both exhibit good behavior for resolution up to 16 km.

#### 4. Vertical velocity and horizontal resolution

In the numerical simulations, the aspect ratio of the convective clouds is primarily determined by the horizontal resolution. In particular, the coarse simulations force the model to produce very flat clouds. A scaling argument is derived here to determine the effect of the aspect ratio on the vertical velocity of an ascending bubble. The scaling law for the idealized bubble is then used to renormalize the PDFs for vertical velocity in the numerical simulations.

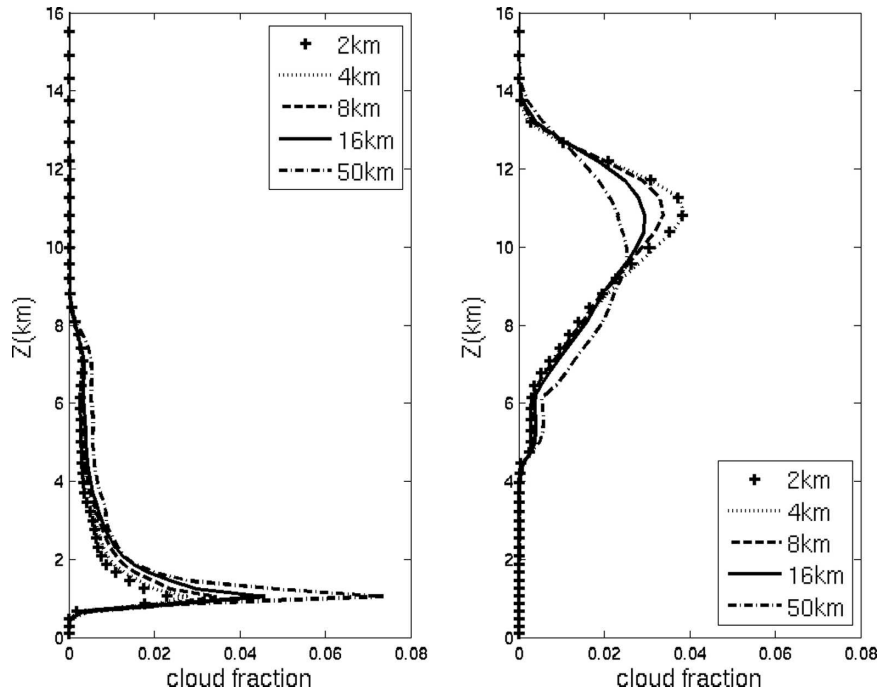


FIG. 8. Cloud fraction for cloud (left) water and (right) ice. Cloud fraction is defined as the probability for the cloud water or ice concentration to exceed  $0.05 \text{ g kg}^{-1}$ . Results shown for resolution of 2 (cross), 4 (dotted line), 8 (dashed line), 16 (solid line), and 50 km (dash-dotted line).

Consider an idealized bubble rising in an environment at rest. If the bubble is less dense than its environment, it will accelerate upward. The buoyancy is equal to the force per unit of mass that would have to be applied in order to prevent the bubble to rise. How-

ever, the buoyancy is not necessarily equal to the vertical acceleration. Indeed, for the bubble to rise, the air above and below it must be displaced. This occurs through the intermediary of a nonhydrostatic pressure field that generates motions away from the bubble and reduces the effective vertical acceleration. Davies-Jones (2003) discusses the relationship between buoy-

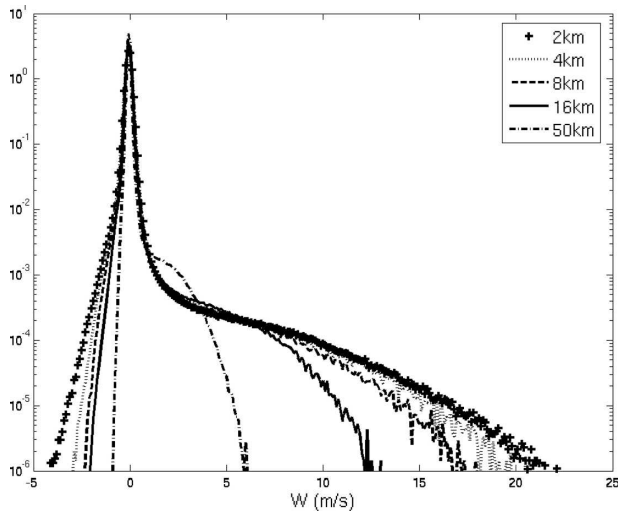


FIG. 9. PDF for the vertical velocity averaged between 4- and 8-km height, for resolution of 2 (cross), 4 (dotted line), 8 (dashed line), 16 (solid line), and 50 km (dash-dotted line).

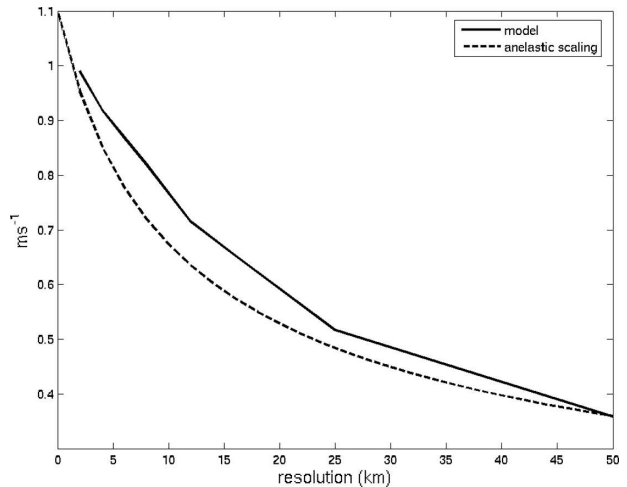


FIG. 10. Third moment of the vertical velocity in the simulation (solid line). It is compared with the nonhydrostatic scaling (19).

ancy and acceleration in an anelastic fluid and finds that acceleration and buoyancy are related through a second-order partial differential equation. Here, rather than deriving an exact three-dimensional solution, a discretized version of the equations of motion is used. The problem reduces then to a second order ordinary differential equation that is used to derive the scale dependency for vertical acceleration and velocity.

Following the Davies-Jones (2003) formulation, the equations of motion for an anelastic fluid are

$$\bar{\rho} \frac{d}{dt} \mathbf{V} = -\nabla p_{nh} - \nabla_H P_h \quad (5)$$

$$\nabla \cdot (\bar{\rho} \mathbf{V}) = 0. \quad (6)$$

Here,  $\mathbf{V}$  is the three-dimensional velocity field,  $d/dt = \partial_t + \mathbf{V} \cdot \nabla$  denotes the Lagrangian derivative,  $\nabla_H = (\partial_x, \partial_y, 0)$  is the horizontal gradient,  $\bar{\rho}(z)$  is the reference density,  $p = p_{nh} + p_h$  is the pressure,  $p_{nh}$  is the local nonhydrostatic component of the pressure field, and  $p_h = \int_z^\infty \rho g dz$  is the local hydrostatic component. Note that in this decomposition, the vertical acceleration due to the hydrostatic pressure field balances exactly the gravitational acceleration (including buoyancy). The vertical momentum equation thus reduces to  $\bar{\rho}(d/dt)w = -\partial_z p_{nh}$ .

The atmosphere is separated into a cylindrical column where the bubble is located and its environment. When the density of the bubble differs from that of the environment, the bubble is subject to a vertical acceleration. The net vertical acceleration depends on both the buoyancy of the bubble and on the geometry of the problem. The primary goal of this exercise is to determine how the bubble's diameter  $L$  affects the effective acceleration. Rather than considering the full system (5)–(6), the equations of motion for the air in the column can be discretized

$$\bar{\rho}(\partial_t w + w \partial_z w) = -\partial_z p_{nh} \quad (7)$$

$$\bar{\rho}(\partial_t U + w \partial_z U) = \frac{P_h + p_{nh} - P_e}{L} \quad (8)$$

$$\frac{\pi L^2}{4} \partial_z (\bar{\rho} w) - \pi L \bar{\rho} U = 0. \quad (9)$$

The discretization assumes that  $w$  is the average velocity through a section of the column,  $U$  is the radial velocity on the later boundary of the column,  $P_h + p_{nh}$  is the total pressure at the center of the column, and  $P_e$  is the pressure in the environment, far away from the column. The pressure in the bubble's column containing the bubble is the sum of a nonhydrostatic pressure perturbation  $p_{nh}$  and the hydrostatic pressure  $P_h(z)$  given by

$$P_h(z) = \int_z^\infty g \rho(z') dz', \quad (10)$$

so that the gravitational acceleration cancels the vertical gradient of the hydrostatic pressure field in (7). For this problem, it is assumed that the environment is in hydrostatic balance. The pressure  $P_e(z)$  in the environment is given by

$$P_e(z) = \int_z^\infty g \rho_e(z') dz'. \quad (11)$$

Neglecting the nonhydrostatic pressure field outside the bubble column is equivalent to treating the environment as an infinite mass reservoir.

The nonhydrostatic pressure can be obtained by multiplying (8) by  $4/L$  and adding the vertical derivative of (7). The continuity equation [Eq. (9)] implies that the sum of the derivative vanishes, which yields

$$\begin{aligned} \partial_{zz} p_{nh} - \frac{4}{L^2} p_{nh} &= \frac{4}{L^2} (P_h - P_e) \\ &\quad - \partial_z \left[ \bar{\rho} \partial_z \frac{w^2}{2} - w \partial_{zz} (\bar{\rho} w) \right]. \end{aligned} \quad (12)$$

When the terms on the right-hand side of the equation are known, the nonhydrostatic pressure field is the solution of an ordinary differential equation. As the differential operator is linear, the nonhydrostatic pressure can be decomposed into a contribution balancing the nonlinear advection terms, and a contribution balancing the hydrostatic pressure term. The latter is obtained by taking the vertical derivative of (12), which yields

$$\partial_{zz} (\partial_z p_{nh}) - \frac{4}{L^2} \partial_z p_{nh} = -g \frac{4}{L^2} (\rho - \rho_e). \quad (13)$$

The vertical acceleration in the column is given by

$$-\frac{1}{\bar{\rho}} \partial_z p_{nh}(z) = \int_0^\infty G(z, z') g \frac{\rho_e - \rho}{\bar{\rho}} dz', \quad (14)$$

where  $G(z, z')$  is the Green function of the differential Eq. (13):

$$\begin{aligned} G(z, z') &= \frac{L}{2} \sinh\left(\frac{2z}{L}\right) \exp\left(-\frac{2z'}{L}\right) \quad \text{for } z \leq z' \\ &= \frac{L}{2} \sinh\left(\frac{2z'}{L}\right) \exp\left(-\frac{2z}{L}\right) \quad \text{for } z > z'. \end{aligned} \quad (15)$$

The integrand in Eq. (14) is given by the product of the Green function and the buoyancy  $b = g(\rho_e - \rho/\bar{\rho})$  of the air in the column. In a nonhydrostatic fluid, the vertical acceleration is a weighted average of the buoyancy in the air column. As an air bubble rises, it

generates a secondary circulation above and below itself. This circulation is produced by the nonhydrostatic pressure field, which redistributes the vertical buoyancy acceleration to a larger portion of the atmosphere in order to ensure the mass conservation. The form of the Green function (15) indicates that the buoyancy acceleration is diluted through a depth equal to the diameter of the bubble, which also corresponds to a secondary circulation of aspect ratio 1.

Consider a bubble of buoyancy  $B$ , diameter  $L$ , and thickness  $\Delta Z$ , which has risen from the surface up to a height  $H$  above the ground. Three cases are considered now: a narrow bubble, a flat bubble high in the atmosphere, and a flat bubble near the surface.

- 1) For a narrow bubble, the Green function converges toward a Dirac function as  $L/\Delta Z \rightarrow 0$ . The vertical acceleration is equal to the buoyancy. In this case, the total kinetic energy imparted to the parcel during its ascent is  $BH$ , and its vertical velocity is therefore

$$w_0 \approx (2BH)^{1/2}. \quad (16)$$

- 2) For a flat bubble, with  $L \gg \Delta Z$ , away from the lower boundary, in the sense that  $H \gg 2L$ , the Green function (15) can be approximated by

$$G(z, z') \approx \frac{L}{4} \exp\left(-\frac{2|z' - z|}{L}\right). \quad (17)$$

The acceleration is approximately equal to the buoyancy averaged over a thickness equal to the horizontal extent of the bubble:

$$\partial_z p_{nh} \approx \frac{B}{1 + \frac{L}{\Delta Z}}, \quad (18)$$

assuming an exponential distribution of buoyancy. If this bubble has risen from the surface to the height  $H$ , its kinetic energy will be given by the total work done by the nonhydrostatic pressure on the bubble:

$$w \approx \left(\frac{2BH}{1 + \frac{L}{\Delta Z}}\right)^{1/2} \approx \left(1 + \frac{L}{\Delta Z}\right)^{-1/2} w_0. \quad (19)$$

Figure 11 shows the third-order moment of the vertical velocity in the simulations as a function of the grid resolution. It shows a very good agreement with the anelastic scaling (19). The value of  $\Delta Z$  here is 6 km. It is worth noting that even for an aspect ratio one bubble, the nonhydrostatic effects result in a vertical velocity that is 40% smaller than that of an infinitely narrow bubble.

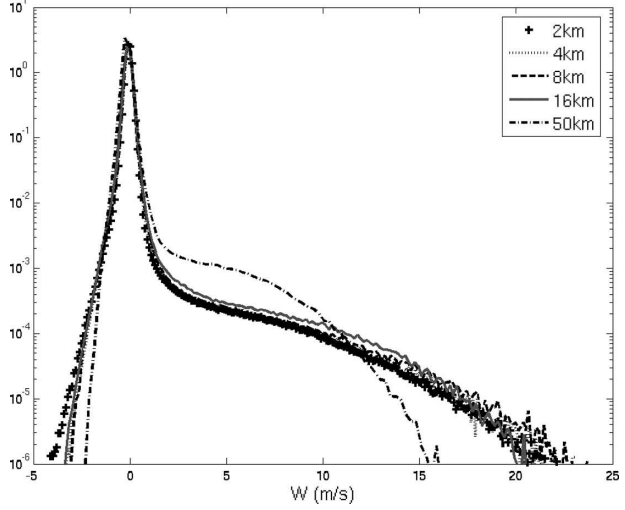


FIG. 11. PDF for the vertical velocity renormalized to the 2km case, using Eq. (24). Results shown for resolution of 2 (cross), 4 (dotted line), 8 (dashed line), 16 (solid line), and 50 km (dash-dotted line).

- 3) For a flat bubble, with  $L \gg \Delta Z$ , near the ground, with  $H \ll L/2$ , the lower boundary acts to reduce the vertical acceleration even further, and the Green function (15) can be approximated by

$$G(z, z') \approx z \exp\left(-\frac{2z'}{L}\right) \quad \text{for } z \leq z'$$

$$\approx z' \exp\left(-\frac{2z}{L}\right) \quad \text{for } z \leq z'. \quad (20)$$

Near the ground, the acceleration of a bubble scales as

$$\partial_z p_{nh} \approx \frac{4B\Delta ZH}{L^2}. \quad (21)$$

The vertical velocity can be approximated by

$$w \approx 2 \frac{(\Delta ZH)^{1/2}}{L} w_0. \quad (22)$$

Physically, the work done during the ascent of a shallow bubble is used to generate the horizontal kinetic energy of the convergent flow under the bubble, with little generation of vertical kinetic energy.

Even when the nonhydrostatic pressure redistributes the vertical acceleration to a larger portion of the fluid, the total work performed by a rising bubble remains equal to the buoyancy flux. In particular, it is independent of the horizontal extent of the bubble. The difference in the resulting vertical velocities are due to the fact that the fraction of this total work used to accelerate the bubble is a function of the geometry of the

problem. The rest of the work is used to sustain the circulation in the surrounding air, and generate vertical and horizontal motions outside the ascending bubble.

In the numerical simulations, the ratio of the generation of vertical kinetic energy to horizontal kinetic energy agrees with a scaling as

$$\frac{\int w \partial_z p}{\int u \partial_x p + v \partial_y p} \approx \frac{L_0}{L},$$

with equipartition occurring for  $L = L_0 \approx 6$  km. This indicates that the ratio of vertical kinetic energy generation to horizontal kinetic energy generation is equal to the ratio of the kinetic energy generation within an ascending bubble to the kinetic energy generation in the environment. This can be explained by the fact that, as the atmosphere is stratified, any environmental air that has been lifted at the same time as the bubble rises will fall back to its original level. Through this process, the vertical kinetic energy is converted into the available potential energy and radiated away. The net production of vertical kinetic energy is equal to the amount required to balance the kinetic energy dissipation in convective air that irreversibly ascends.

Many large-scale models make use of the hydrostatic approximation to simplify the vertical momentum equation. As a result, the work required for accelerating a parcel in the vertical direction is neglected. All mechanical energy produced during a parcel's ascent is used to generate horizontal kinetic energy, independent of the resolution. As the horizontal velocity is independent of the grid resolution, the vertical velocity is inversely proportional to the grid resolution for a hydrostatic model:

$$w_{\text{hyd}} \approx \frac{H}{L} w_0. \quad (23)$$

At resolutions much larger than the depth of the troposphere, the parcel always feels the influence of the lower boundary, and the appropriate nonhydrostatic scaling (22) predicts the same dependency on the horizontal resolution as the hydrostatic scaling (23). However, for resolutions finer than the depth of the troposphere, the effects of the lower boundary are less significant, and the nonhydrostatic scaling (19) applies. In this case, the nonhydrostatic scaling is much less sensitive to changes in the horizontal resolution than the equivalent hydrostatic scaling. For a horizontal resolution equal to or smaller than the depth of the tropopause, the hydrostatic approximation leads to a significant, and unrealistic, increase of the vertical velocity.

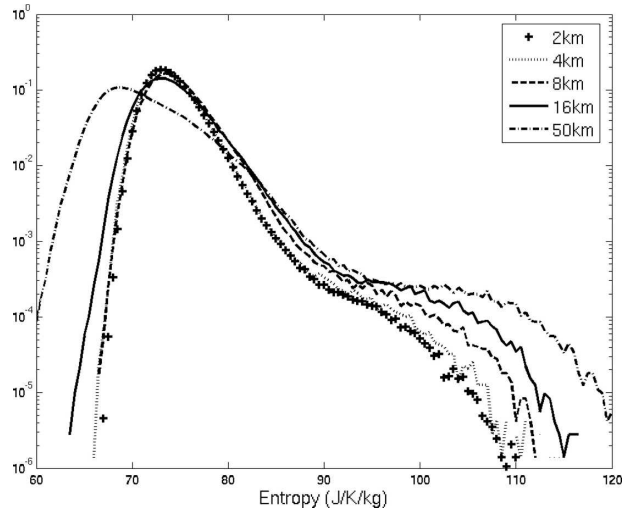


FIG. 12. PDF for moist entropy at 6-km vertical velocity renormalized to the 2-km case, for resolution of 2 (cross), 4 (dotted line), 8 (dashed line), 16 (solid line), and 50 km (dash-dotted line).

These arguments can be used to rescale the probability distribution function. If  $f(w, r_0)$  is the value of the PDF for vertical velocity  $w$  at resolution  $r_0$ , then the rescaling of the PDF  $f_R$  to a resolution  $r_1$  is given by

$$f_R(w, r_1) = \alpha(r_1, r_0) f(\alpha(r_1, r_0)^{-1} w, r_0). \quad (24)$$

Here,  $\alpha(r_1, r_0)$  is the ratio of the typical velocity between resolution  $r_0$  and  $r_1$ , derived from (19):

$$\alpha(r_1, r_0) = \left( \frac{1 + \frac{r_0}{\Delta Z}}{1 + \frac{r_1}{\Delta Z}} \right)^{1/2}. \quad (25)$$

This rescaling is applied to the PDFs obtained in section 3. The only unknown is  $\Delta Z$ , which should be interpreted as the vertical extent of a typical updraft. A value of  $\Delta Z = 6$  km has been used, which corresponds to the resolution at which the production of kinetic energy is equally divided between the vertical and horizontal component in the simulations. The PDFs rescaled to the 2-km resolution are shown in Fig. 12. There is a very close match between the rescaled PDFs. Only the 25- and 50-km cases differ significantly, which is not surprising given that at such coarse resolution, the ascending parcel should feel the effect of the lower boundary, so that the scaling (22) would become more appropriate.

The scaling laws discussed in this section are based on two central assumptions about the behavior of a convective tower. First, it requires that the buoyancy of an ascending air parcel is unaffected by the horizontal

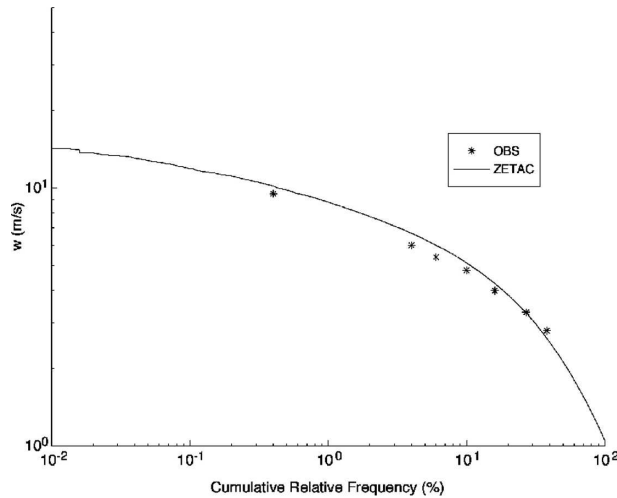


FIG. 13. Cumulative probability spectrum for the vertical velocity during the GATE experiment from numerical simulations with the Zetac model (solid line), and observations (cross) from LeMone and Zipser (1980).

resolution in the simulation. This implies that the thermodynamic and microphysical properties of the updrafts remain similar through the various experiments. This is verified by analyzing the PDF for entropy shown in Fig. 13. While there is a slight widening of the PDF at coarse resolution, this change is quite small in comparison to the difference between the updraft and their environment. This would not have been the case if, for example, entrainment in the updraft was strongly affected by the grid size. Second, it assumes that the size of the updraft is determined by the grid resolution. In particular, this implies that the scaling should not hold for very high-resolution simulations of convection, in which the horizontal extent of the updraft would be determined by the internal turbulence.

## 5. Conclusions

In this paper, the impact of horizontal resolution on the behavior of simulated convection has been investigated. Simulations of an idealized radiative–convective equilibrium were performed for resolutions varying between 2 to 50 km. The simulations were run for 16 days, and the analysis focuses primarily on the long-term statistical behavior of the simulated convection. This setup is designed to evaluate whether a coarse nonhydrostatic model could be used adequately to simulate the behavior of moist convection in climate models.

On the negative side, it was found that the shallow convection in the model is very sensitive to the horizontal resolution. This sensitivity is most apparent in the distribution of cloud water at low levels, and in the

lower tropospheric humidity. Coarse resolution models cannot represent the overturning in shallow convection. Rather, they produce a significant amount of flat stratiform clouds that do not mix with the environment. As a consequence, there is very little mixing between the boundary layer and the troposphere. This also leads a dry bias in the lower troposphere at coarse resolution. Improving the representation of shallow clouds is the main benefit of an increased resolution.

On the positive side, the behavior of deep convective tower is much more robust. The vertical velocity showed a limited sensitivity to horizontal resolution. For example, the third moment of vertical velocity in the 16-km resolution simulations is only one-half of that obtained with a 2-km resolution. This low sensitivity of the vertical velocity is also associated with good behavior for cirrus clouds. Indeed, the PDFs for cloud ice show only small sensitivity for resolutions up to 16 km. Overall, these results indicate a robust behavior of deep convective towers, including their outflow, over a wide range of resolutions.

A theoretical scaling has been derived to explain the low but nonnegligible sensitivity of the vertical velocity to horizontal resolution. The analysis of the vertical acceleration of an idealized bubble indicates that the nonhydrostatic pressure fields acts to spread the buoyancy acceleration of a flat bubble to a much deeper portion of the air column. This leads to a dissolution of the vertical acceleration, and a weaker vertical velocity. The scaling obtained shows that the vertical velocity varies approximately as  $(1 + L/\Delta Z)^{-1/2}$ , for a bubble away from the lower boundary, with  $\Delta Z/L$  the aspect ratio of the bubble. In terms of the numerical simulation, this scaling implies that the vertical velocity varies at most as one over the square root of the horizontal grid space for the range of resolutions considered in this study.

A very promising result lies in the possibility of using the theoretical scaling arguments to rescale the vertical velocity in coarse resolution simulations. It was shown that the PDF of the high-resolution simulation could be obtained by renormalizing the PDFs of coarser simulation. Hence, the scaling law proposed here could potentially be used to improve the behavior of deep convection simulated with models of horizontal resolutions in the range of 5 to 20 km

## APPENDIX

### Numerical Model Description

The prognostic variables are the three-dimensional velocity,  $\mathbf{V} = (u, v, w)$ , the potential temperature  $\theta$ , the specific humidity  $q_v$ , five species of condensed water

(cloud water, cloud ice, rain, graupel, and snow), and the Exner function,  $\pi = (p/p_0)^{R/C_p}$ , where  $p_0$  is a constant reference pressure. The dynamical equations in Cartesian coordinates with no topography or rotation are

$$\frac{d}{dt}u = -C_p\theta_v(1+q_c)^{-1}\partial_x\pi + D_u, \quad (\text{A1})$$

$$\frac{d}{dt}v = -C_p\theta_v(1+q_c)^{-1}\partial_y\pi + D_v, \quad (\text{A2})$$

$$\frac{d}{dt}w = -(C_p\theta_v\partial_z\pi + g)(1+q_c)^{-1} + D_w, \quad (\text{A3})$$

$$\frac{d}{dt}\theta = \frac{Q}{C_p\pi} + D_\theta, \quad (\text{A4})$$

$$\frac{d}{dt}q_v = E + D_q, \quad (\text{A5})$$

$$\frac{d}{dt}\pi = -\frac{R\pi}{C_v}\pi(\nabla \cdot \mathbf{V} - E) + \frac{R\pi}{C_v\theta_v}\frac{d}{dt}\theta_v. \quad (\text{A6})$$

Here  $D$  is the tendency due to subgrid-scale diffusion,  $q_c$  is the total condensate,  $Q$  is the diabatic forcing (including latent heat release),  $E$  is the net conversion of condensed water into water vapor,  $g$  is the gravitational acceleration, and  $\theta_v = \theta(1 + 0.608q_v)$  is the virtual potential temperature. The Lagrangian derivative is  $d/dt = \partial/\partial t + \mathbf{V} \cdot \nabla$ . The tendency for the Exner function (A6) is derived from the continuity equation

$$\frac{d}{dt}\rho = -\rho(\nabla \cdot \mathbf{V} - E),$$

together with the ideal gas law

$$\pi^{C_v/R} = \frac{\rho\theta_v}{p_0}.$$

The tendency for the Exner function can be manipulated into an equivalent flux form:

$$\frac{\partial\pi}{\partial t} = \mu^{-1}\pi\left(-\frac{\nabla \cdot \pi^\mu\mathbf{V}}{\pi^\mu} + \theta_v^{-1}\frac{d}{dt}\theta_v\right), \quad (\text{A7})$$

or

$$\frac{\partial\pi}{\partial t} = \mu^{-1}\pi\left(-\frac{\nabla \cdot \rho\mathbf{V}}{\rho} + \theta_v^{-1}\frac{\partial\theta_v}{\partial t}\right), \quad (\text{A8})$$

with  $\mu = C_v/R$ .

The microphysical parameterization is that of Lin et al. (1983), as modified by Lord et al. (1984) and Krueger et al. (1995). The diffusion term is obtained from a three-dimensional turbulent kinetic energy scheme similar to that of Klemp and Wilhelmson (1978), and the surface fluxes are obtained from a Monin–Obukhov implementation described in Anderson et al. (2004). The surface roughness calculation incorporates a diag-

nosis of wave heights according to the method of Beljaars (1995).

The numerical solution is obtained using leapfrog time stepping and centered space derivatives on a C grid. Advective tendencies are computed according to the PPM in all three directions for all variables (Colella and Woodward 1984). For the Exner function forecast, PPM is applied to the combined flux term as it appears in (A7).

Following Klemp and Wilhelmson (1978), we increase the computational efficiency of the dynamical core by evaluating a linearized form of the source terms on a fast time step. A height-dependent reference state, denoted by an overbar, is chosen so that the following linear tendencies due to acoustic gravity waves can be evaluated on the fast step:

$$\frac{\partial u}{\partial t} = -C_p\bar{\theta}_v(1+q_c)^{-1}\frac{\partial\pi}{\partial x}, \quad (\text{A9})$$

$$\frac{\partial v}{\partial t} = -C_p\bar{\theta}_v(1+q_c)^{-1}\frac{\partial\pi}{\partial y}, \quad (\text{A10})$$

$$\frac{\partial w}{\partial t} = \left(g\frac{\theta_v - \bar{\theta}_v}{\theta_v} - C_p\bar{\theta}_v\frac{\partial}{\partial x}(\pi - \bar{\pi})\right)(1+q_c)^{-1}, \quad (\text{A11})$$

$$\frac{\partial\pi}{\partial t} = -\mu^{-1}\bar{\pi}^{1-\mu}\nabla \cdot (\pi^\mu\mathbf{V}), \quad (\text{A12})$$

$$\frac{\partial\theta_v}{\partial t} = -\mathbf{V} \cdot \nabla\bar{\theta}_v. \quad (\text{A13})$$

Here  $\bar{\pi}(z)$  is in hydrostatic balance with the reference profile of virtual potential temperature  $\bar{\theta}_v$ ; thus  $(\partial/\partial z)\bar{\pi} = -(g/C_p\bar{\theta}_c)$ . The linearization of the Exner Eq. (A12) is based on (A7). The Lagrangian tendency of  $\theta_v$  is added on the slow time step. What remains on the right-hand side of (A1)–(A5) and (A7) after these terms are subtracted is frozen during the fast cycle. The moisture variables  $q_v$  and  $q_c$  are also frozen. As a result, the original slow time step is not constrained by internal wave propagation.

The terms on the rhs of (A9)–(A13) are subtracted at the slow time and evaluated at the fast time. Thus, for example, the full equation for virtual potential temperature, combining (A4), (A5), and (A13), is

$$\frac{\partial\theta_v}{\partial t} = -\mathbf{V}_s \cdot \nabla\theta_v - (\mathbf{V}_f - \mathbf{V}_s) \cdot \nabla\bar{\theta}_v + Q_v, \quad (\text{A14})$$

where subscripts  $s$  and  $f$  refer to slow and fast, and  $Q_v = Q(1 + 0.608q_v) + 0.608\theta E$  (evaluated on the slow time). This departs from the original method of Klemp and Wilhelmson (1978) not only by including the gravity wave terms in the fast time step but also by retaining

the full advection in the slow tendency. This takes better advantage of sophisticated algorithms for advection such as PPM.

The fast time step is constrained by acoustic gravity waves. To relax this constraint without significantly diminishing the accuracy of the solution, the vertical propagation is treated semi-implicitly, as in Klemp and Wilhelmson. Vertical sound wave propagation is due to the vertical derivatives in (A11) and (A12). The vertical advection of buoyancy, on the rhs of (A13), is included in the semi-implicit part of the calculation in order to remove the constraint due to vertical gravity wave propagation.

The model has been evaluated against several computational and observational test cases, including Global Atmospheric Research Program Atlantic Tropical Experiment (GATE; e.g., Donner et al. 1999), Tropical Ocean Global Atmosphere Program–Coupled Ocean–Atmosphere Response Experiment (TOGA COARE; e.g., Redelsperger et al. 2000), and Atmospheric Radiation Measurement (ARM; e.g., Xu et al. 2002). The results from Zetac have been compared to found to perform similarly to other CSRMs used in the GEWEX Cloud Systems Study (GCSS; L. J. Donner 2005, personal communication). Figure 13 shows a comparison between observed (from LeMone and Zipser 1980) and modeled cumulative probability distributions of in-cloud vertical velocity for the GATE observing period of 30 August to 16 September 1974. The result demonstrates the ability of the dynamical model and microphysical parameterization to capture this important measure of tropical convection.

#### REFERENCES

- Anderson, J. L., and Coauthors, 2004: The new GFDL global atmosphere and land model AM2–LM2: Evaluation with prescribed SST simulations. *J. Climate*, **17**, 4641–4673.
- Arakawa, A., 2004: The cumulus parameterization problem: Past, present, and future. *J. Climate*, **17**, 2493–2524.
- , and W. H. Schubert, 1974: Interaction of a cumulus cloud ensemble with the large-scale environment, Part I. *J. Atmos. Sci.*, **31**, 674–701.
- Beljaars, A. C. M., 1995: The parameterization of surface fluxes in large-scale models under free convection. *Quart. J. Roy. Meteor. Soc.*, **121**, 255–270.
- Betts, A. K., and M. J. Miller, 1986: New convective adjustment scheme. Pt. 2. Single column tests using GATE wave, BOMEX, ATEX, and Arctic air-mass data sets. *Quart. J. Roy. Meteor. Soc.*, **112**, 693–709.
- Bryan, G. H., J. C. Wyngaard, and J. M. Fritsch, 2003: Resolution requirements for the simulation of deep moist convection. *Mon. Wea. Rev.*, **131**, 2394–2416.
- Colella, P., and P. R. Woodward, 1984: The piecewise parabolic method (PPM) for gas-dynamical simulations. *J. Comput. Phys.*, **54**, 174–201.
- Davies-Jones, R., 2003: An expression for effective buoyancy in surroundings with horizontal density gradients. *J. Atmos. Sci.*, **60**, 2922–2925.
- Donner, L. J., C. J. Seman, and R. S. Hemler, 1999: Three-dimensional cloud-system modeling of GATE convection. *J. Atmos. Sci.*, **56**, 1885–1912.
- Emanuel, K. A., 1991: A scheme for representing cumulus convection in large-scale models. *J. Atmos. Sci.*, **48**, 2313–2329.
- , and M. Bister, 1996: Moist convective velocity and buoyancy scales. *J. Atmos. Sci.*, **53**, 3276–3285.
- Grabowski, W., 2001: Coupling cloud processes with the large-scale dynamics using the Cloud-Resolving Convection Parameterization (CRCP). *J. Atmos. Sci.*, **58**, 978–997.
- Jung, J.-H., and A. Arakawa, 2004: The resolution dependence of model physics: Illustrations from nonhydrostatic model experiments. *J. Atmos. Sci.*, **61**, 88–102.
- Klemp, J. B., and R. B. Wilhelmson, 1978: The simulation of three-dimensional convective storm dynamics. *J. Atmos. Sci.*, **35**, 1070–1096.
- Krueger, S. K., K. N. Liou, Q. Fu, and H.-N. S. Chin, 1995: Improvements of an ice-phase microphysics parameterization for use in numerical simulations of tropical convection. *J. Appl. Meteor.*, **34**, 281–287.
- LeMone, M. A., and E. J. Zipser, 1980: Cumulonimbus vertical velocity events in GATE. Part I: Diameter, intensity and mass flux. *J. Atmos. Sci.*, **37**, 2444–2457.
- Lin, Y.-L., R. D. Farley, and H. D. Orville, 1983: Bulk parameterization of the snow field in a cloud model. *J. Appl. Meteor.*, **22**, 1065–1092.
- Liu, C., M. W. Moncrieff, and W. W. Grabowski, 2001: Hierarchical modeling of tropical convective systems using explicit and parameterized approaches. *Quart. J. Roy. Meteor. Soc.*, **127**, 493–515.
- Lord, S. J., H. E. Willoughby, and J. M. Piotrowicz, 1984: Role of a parameterized ice-phase microphysics in an axisymmetric, nonhydrostatic tropical cyclone model. *J. Atmos. Sci.*, **41**, 2836–2848.
- Lorenz, E., 1975: Climatic predictability. *The Physical Basis of Climate and Climate Modelling*, B. Bolin et al., Eds., GARP Publication Series, Vol. 16, World Meteorological Organization, 132–136.
- Manabe, S., J. Smagorinsky, and R. F. Strickler, 1965: Simulated climatology of a general circulation model with a hydrological cycle. *Mon. Wea. Rev.*, **93**, 769–798.
- Pauluis, O., and I. M. Held, 2002a: Entropy budget of an atmosphere in radiative–convective equilibrium. Part I: Maximum work and frictional dissipation. *J. Atmos. Sci.*, **59**, 125–139.
- , and —, 2002b: Entropy budget of an atmosphere in radiative–convective equilibrium. Part II: Latent heat transport and moist processes. *J. Atmos. Sci.*, **59**, 140–149.
- Randall, D. A., M. Khairoutdinov, A. Arakawa, and W. Grabowski, 2003: Breaking the cloud parameterization deadlock. *Bull. Amer. Meteor. Soc.*, **84**, 1547–1564.
- Redelsperger, J. L., and Coauthors, 2000: A GCSS model intercomparison for a tropical squall line observed during TOGA-COARE. 1. Cloud-resolving models. *Quart. J. Roy. Meteor. Soc.*, **126**, 823–863.
- Satoh, M., H. Tomita, H. Miura, S. Iga, and T. Nasun, 2005: Development of a global cloud resolving model a multi-scale structure of tropical convections. *J. Earth Simul.*, **3**, 1–9.
- Xu, K.-M., and Coauthors, 2002: An intercomparison of cloud-resolving models with the Atmospheric Radiation Measurement summer 1997 Intensive Observation Period data. *Quart. J. Roy. Meteor. Soc.*, **128**, 593–624.